ЖЭТФ, 2011, том 140, вып. 5 (11), стр. 961–967 

# PROTON NMR STUDY OF THE ORGANIC METAL $\kappa$-$(BETS)_2Mn[N(CN)_2]_3$

***O. M. Vyaselev*** [a]*, ***N. D. Kushch*** [b], ***E. B. Yagubskii*** [b]

[a] *Institute of Solid State Physics, Russian Academy of Sciences*
*142432, Chernogolovka, Moscow Region, Russia*

[b] *Institute of Problems of Chemical Physics, Russian Academy of Sciences*
*142432, Chernogolovka, Moscow Region, Russia*

Received March 10, 2011

Magnetic properties of the organic conductor $\kappa$-$(BETS)_2Mn[N(CN)_2]_3$ above and below the temperature of the metal–insulator transition that occurs at $T_{MI} \approx 25$ K are studied by $^1$H NMR. The proton spectrum is shown to be determined by the static dipolar fields from $Mn^{2+}$ localized moments, while the $^1$H spin–lattice relaxation is dominated by fluctuating fields from $Mn^{2+}$ electrons. The NMR data, both static (the spectra) and dynamic (the spin–lattice relaxation), indicate the freezing of $Mn^{2+}$ moments into a short-range or an incommensurate long-range antiferromagnetic order below $T_{MI}$.

## 1. INTRODUCTION

One of the modern trends in the physics of organic conductors is manufacturing of bifunctional materials by fusing the conducting and magnetic properties within the same crystal lattice. This can be achieved, for instance, by synthesizing the radical cation salts of organic $\pi$-donors that provide the quasi-two-dimensional conductivity, with paramagnetic metal complex anions [1–5]. In such compounds, interaction between the localized spins of $d$-electrons in insulating magnetic layers and itinerant spins of the $\pi$-band electrons in conducting organic layers (the $\pi$–$d$ interaction) gives rise to interesting phenomena like the field-induced superconductivity observed in $\lambda$-$(BETS)_2FeCl_4$ [6] and $\kappa$-$(BETS)_2FeBr_4$ [7], where BETS stands for $C_{10}S_4Se_4H_8$, bis(ethylenedithio)tetraselenafulvalene. The complex $\kappa$-$(BETS)_2Mn[N(CN)_2]_3$ addressed in this paper is one of the newest members of this family. Its remarkable feature is an extremely pressure-sensitive metal–insulator (MI) transition [8]. This transition that occurs at the temperature $T_{MI} \approx 25$ K at ambient pressure can be suppressed by applying a relatively low external pressure, yielding a superconducting state with the maximum $T_c = 5.75$ K at $P = 0.6$–$1.0$ kbar [9].

The question about the role of the interaction between itinerant spins of the donor layers and localized spins of the insulating magnetic layers in the formation of the insulating ground state in the above compounds is still open. In $\lambda$-$(BETS)_2FeCl_4$, where the MI transition coexists with the onset of the pronounced Néel-type antiferromagnetic (AF) order [10–12], the localization of $\pi$-electrons has been suggested to result from magnetic ordering within the $Fe^{3+}$ subsystem [13]. On the contrary, the magnetic properties of $\kappa$-$(BETS)_2Mn[N(CN)_2]_3$ in the insulating state are not obvious enough to unambiguously claim the long-range AF order in the $Mn^{2+}$ subsystem [8]. This raises doubts concerning the above localization scenario for this compound, favoring the Mott localization usual for quasi-two-dimensional organic compounds with the narrow half-filled conducting band [14].

In this paper, we report the results of a $^1$H NMR study of $\kappa$-$(BETS)_2Mn[N(CN)_2]_3$ undertaken to probe its magnetic structure below the MI transition and reveal its possible role in the localization of $\pi$-electrons.

## 2. EXPERIMENTAL

The crystal structure of $\kappa$-$(BETS)_2Mn[N(CN)_2]_3$ is monoclinic with the space group $P2_1/c$ and the lattice constants at 88 K given by $a = 19.428$ Å, $b = 8.379$ Å, $c = 11.869$ Å, $\beta = 92.67°$, and $V = 1930.1$ Å$^3$, with two

*E-mail: vyasel@issp.ac.ru

formula units per unit cell [9]. The conducting layers formed by BETS dimers in the $bc$ plane are sandwiched between the polymeric $Mn[N(CN)_2]_3$ anion layers in the $a$ direction. The crystal growth procedure and details of the structure have been described previously [8, 9].

One single crystal of the size $a^* \times b \times c \approx 0.05 \times \times 3 \times 1$ mm$^3$ ($a^*$ is the normal to the $bc$ plane) was used for the measurements. The sample was attached to a semicylinder quartz holder with a pin-touch of silicon grease. The $b$ axis of the sample was aligned with the holder axis. One end of the holder was fixed in a goniometer wheel perpendicular to the magnetic field direction. No spurious $^1$H NMR signal from the empty holder with the grease was observed on the scale of the signal from the sample. NMR spectra were acquired with Bruker MSL-300 spectrometer in fields 1.40924 and 6.999 T (for brevity, referred to as 1.4 and 7 T in what follows). A standard spin-echo sequence $\pi/2 - t - \pi - t$ was used, with the $\pi$-pulse length less or equal to 3 $\mu$s, the $t$-delay of 15 $\mu$s, and the recycle delay of 25 ms. To cover the wide-range spectra, the Fourier transforms of the acquired spin-echo second halves were collected at intervals less or equal to 150 kHz and summed up. The nuclear spin–lattice relaxation rate was measured using the standard inversion-recovery pulse sequence $\pi - t_r - \pi/2 - t - \pi - t$.

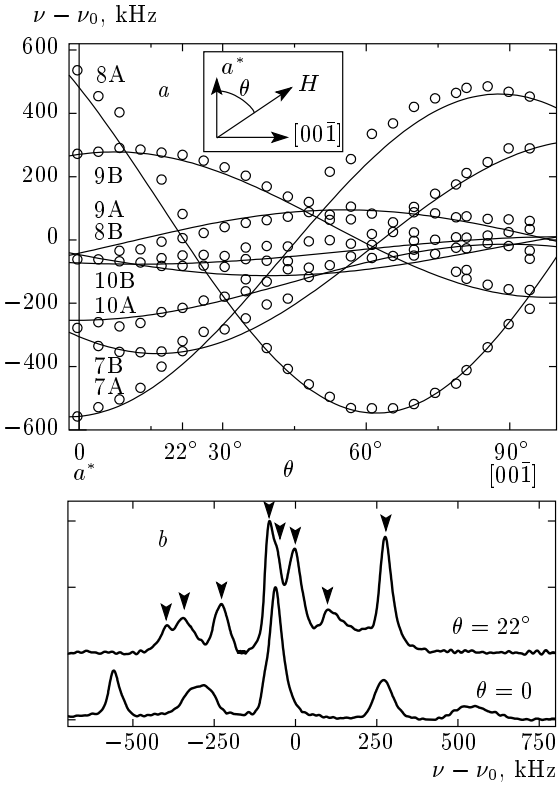


**Fig. 1.** ($a$) Angular evolution of the $^1$H NMR spectrum in the $a^*c$ plane. Circles are the measured peak positions. Lines are the model calculations using Eqs. (1). The indices from 7A through 10B label the hydrogen sites shown below in Fig. 5. ($b$) $^1$H NMR spectra in $\kappa$-$(BETS)_2Mn[N(CN)_2]_3$ at $T = 74$ K in the field $H = 7$ T oriented parallel to $a^*$ ($\theta = 0$) and at $\theta = 22°$ from $a^*$ toward the $[00\bar{1}]$ direction

## 3. RESULTS AND DISCUSSION

### 3.1. $^1$H NMR spectrum

The angular evolution of $^1$H NMR peak positions in $\kappa$-$(BETS)_2Mn[N(CN)_2]_3$ measured at 74 K in the field $H = 7$ T rotated in the $a^*c$ plane is presented in Fig. 1$a$. The peak positions are given with respect to $\nu_0 = \gamma_I H$, where $\gamma_I = 42.5759$ MHz/T is the proton gyromagnetic ratio. The example spectra measured at $\mathbf{H} \parallel \mathbf{a}^*$ and at the angle $\theta = 22°$ from $a^*$ are shown in Fig. 1$b$. Depending on the field direction, the spectrum contains up to eight resonance peaks (shown by arrows on the spectrum for $\theta = 22°$ in Fig. 1$b$), in compliance with the number of inequivalent crystallographic hydrogen sites that belong to the ethylene groups at the terminals of BETS molecules.

The evolution of the $^1$H NMR spectrum ($H = 1.4$ T parallel to $a^*$) with temperature is shown in Fig. 2. As can be seen, the frequency span of the spectrum increases with decreasing temperature, while its shape is maintained down to 20 K. At lower temperatures, the peaks broaden rapidly, which is more pronounced on the right-hand side of the spectrum. Figure 3 shows the temperature dependence of the half width at half height, $\Delta_{1/2}/2$, for the leftmost and the rightmost peaks in the $^1$H NMR spectrum measured at $H = 1.4$ T parallel to $a^*$. As can be seen from Fig. 3, the linewidth is relatively flat above $T_{MI} = 25$ K (especially for the leftmost peak) and increases sharply below this temperature.

To describe the observed peculiarities of the $^1$H NMR spectrum, we start with comparing the temperature dependence of the resonance peaks with that of the dc magnetization. Figures 4$a$ and 4$b$ show temperature dependences of the molar dc magnetization normalized to the applied field, $M/H$, and the frequency shift of the leftmost peak in the spectrum normalized to the Larmour frequency, $\nu/\nu_0 - 1$, measured in the $\mathbf{H} \parallel \mathbf{a}^*$ geometry in the fields 1.4 and 7 T. Figure 4$c$ plots $\nu - \nu_0$ as a function of the magnetization measured at the same temperatures and fields. It has been shown in Ref. [15] that the dc magnetiza-

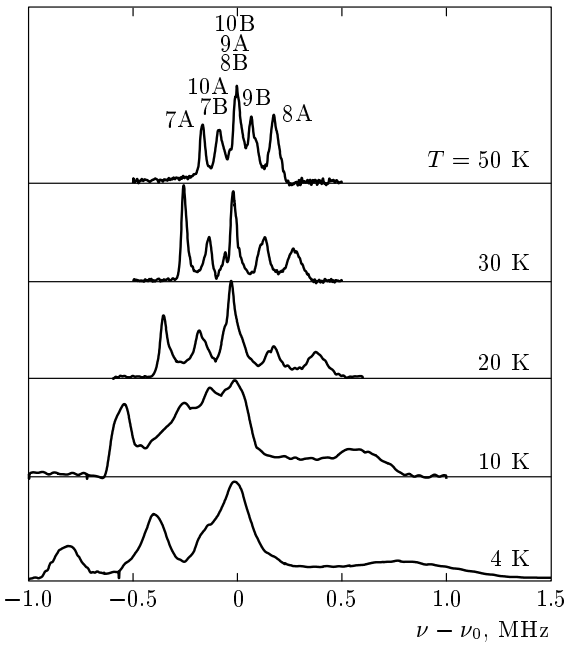


**Fig. 2.** Temperature evolution of the $^1$H NMR spectrum measured at $H = 1.4$ T parallel to $a^*$. The peaks are labeled according to the spectrum simulation in Fig. 1

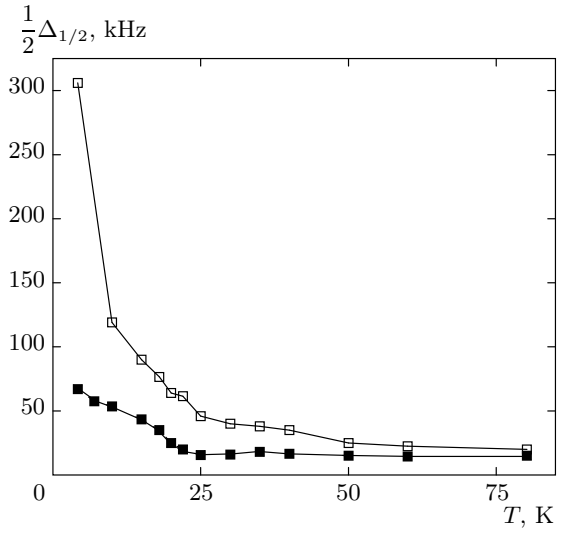


**Fig. 3.** Temperature dependence of the half-linewidth of the leftmost (■) and the rightmost (□) peaks (respectively corresponding to hydrogen sites 7A and 8A) at $H = 1.4$ T parallel to $a^*$

tion in $\kappa$-$(BETS)_2Mn[N(CN)_2]_3$ is determined by $Mn^{2+}$ ($S = 5/2$, $L = 0$) magnetic moments. Therefore, the linearity of the data in Fig. 4*c* demonstrates that for the whole temperature and field ranges covered in the

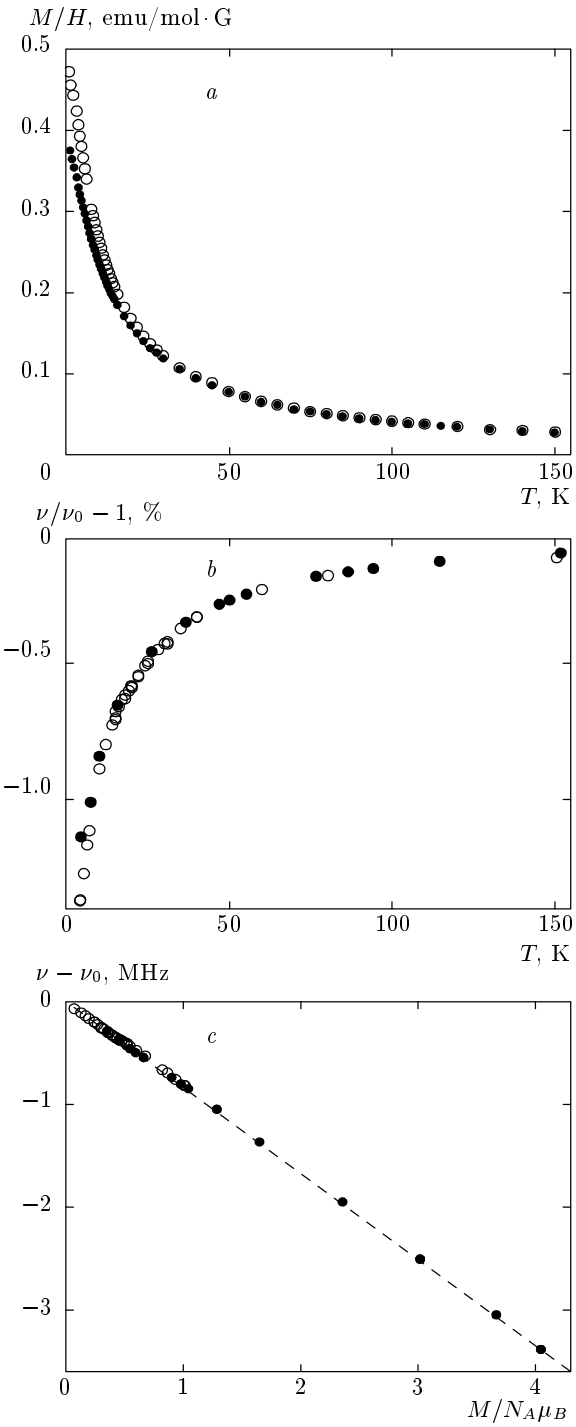


**Fig. 4.** Temperature dependences of the molar magnetization (*a*) and the peak position (*b*) at $H = 1.4$ T (○) and $H = 7$ T (●) and the position of the leftmost peak in the $^1$H NMR spectrum in the fields $H = 1.4$ T (○) and $H = 7$ T (●) parallel to $a^*$ for the temperature range 4–150 K as a function of the dc magnetization per Mn ion $\mu_{Mn} = M/N_A$ measured at the same temperatures and fields and expressed in terms of the Bohr magneton (*c*)

experiment, the $^1$H NMR spectrum peak positions are determined by the magnetic subsystem associated with the $Mn^{2+}$ moments.

Next, we proceed with modeling the spectrum at high temperatures to reproduce its angular behavior shown in Fig. 1. To model the spectrum, we need to sum up all possible hyperfine and dipolar fields at the nucleus site and take into account the Lorentz field $h_{Lor}$ and the sample geometry resulting in a demagnetizing field $h_D$ [16]. However, in the specific case of $^1$H NMR in organic metals [16, 17], the hyperfine fields are negligible compared to the dipolar field $h_{dip}$ from the $Mn^{2+}$ electronic spin. Therefore, for the magnetic field in the $a^*c$ plane, $\mathbf{H} = [H\cos\theta, 0, H\sin\theta]$, we model the spectrum as

$$\nu - \nu_0 = \gamma_I(h_{dip} + h_{Lor} - h_D), \tag{1a}$$

$$h_{dip} = \mu_{\mathrm{Mn}} \sum_i \frac{3\cos^2\alpha_i - 1}{r_i^3}, \tag{1b}$$

$$h_{Lor} = \frac{4\pi}{3}\frac{\mu_{\mathrm{Mn}}}{V_{\mathrm{Mn}}}, \quad h_D = 4\pi N \frac{\mu_{\mathrm{Mn}}}{V_{\mathrm{Mn}}}. \tag{1c}$$

Here, $\mu_{\mathrm{Mn}}$ is the thermal average of the $Mn^{2+}$ magnetic moment projection on the field direction, $r_i$ is the length of the position vector from the proton site to the Mn site $i$, $\alpha_i$ is the angle between this vector and the field direction, $V_{\mathrm{Mn}}$ is the unit cell volume per $Mn^{2+}$ ion, and $N = N_\perp \cos^2\theta + N_\parallel \sin^2\theta$ is the demagnetization factor.

Since the dc magnetization in $\kappa$-$(BETS)_2Mn[N(CN)_2]_3$ is determined by $Mn^{2+}$ magnetic moments, we put $\mu_{\mathrm{Mn}} = M/N_A$ in Eqs. (1), where $M$ is the measured dc magnetization per mole (3800 emu/mol at $H = 7$ T, $T = 74$ K) and $N_A$ is the Avogadro number. For our very thin plate sample, we assume the demagnetization factors $N_\perp = 1$, $N_\parallel = 0$. Crystallographic positions of Mn and H atoms (Fig. 5) required to calculate Eq. (1b) are available online from the Cambridge Crystallographic Data Centre [18]. The sum in Eq. (1b) has been taken over 200 Mn sites within $\pm 20$ Å to provide reasonable convergence.

The peak positions calculated using Eqs. (1) for each of the 8 crystallographically inequivalent hydrogen sites are shown as functions of the field polar angle $\theta$ by solid lines in Fig. 1*a*. The indices (from 7A through 10B) labeling hydrogen sites correspond to those in Ref. [18]. The agreement between the calculated and the measured spectra is clearly reasonable despite the absence of any fitting parameters used in the calculations.

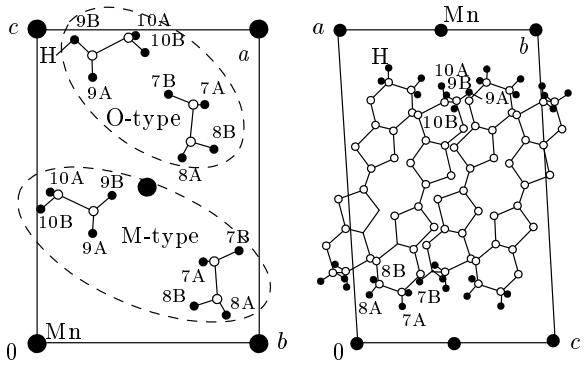


**Fig. 5.** Arrangement of Mn (large black circles) and H (small black circles) atoms within the unit cell. N[$(CN)_2$] bridges are omitted. Hydrogen atoms are labelled according to Ref. [18]; *a* — the BETS molecules and Mn, the *ac*-plane projection; *b* — the *bc*-plane projection. $CH_2$ groups nearest to the anion (Mn) layer are only shown for simplicity. The O- and M-type $CH_2$ groups belong to the corresponding symmetry types of BETS molecules

This model calculation yields two important results. First, the resonance peaks in the spectrum are now identified with certain hydrogen sites (see Fig. 5), which are to be used in what follows. Second, together with the plot shown in Fig. 4, the calculation proves that $^1$H NMR spectral peak positions in $\kappa$-$(BETS)_2Mn[N(CN)_2]_3$ are determined by the dipolar fields from $Mn^{2+}$ moments.

To address the $^1$H NMR linewidth behavior shown in Fig. 3, we need a brief excursion into the crystallography of $\kappa$-$(BETS)_2Mn[N(CN)_2]_3$. From the magnetic viewpoint, symmetry operations of the space group $P2_1/c$ divide the BETS molecules into two types. Molecules of the first type (hereafter referred to as O-type, with "O" for "original") are those with the atom positions at the origin $(x, y, z)$ and produced by inversion $(-x, -y, -z)$. The atoms of the second-type molecules are in positions $(-x, 1/2 + y, 1/2 - z)$ and $(x, 1/2 - y, 1/2 + z)$ produced by a 2-fold screw axis with direction [010] and a glide plane normal to [010]. We note that the $y$-component of the magnetic field, $H_y$, appears for the second-type molecules as $-H_y$. We therefore refer to this kind of molecules as M-type, with "M" for "mirror". The arrangement of the ethylene groups belonging to the two symmetry types of the BETS molecules within the unit cell are shown in Fig. 5.

The above symmetry considerations show that only for the field strictly in the *ac* plane, each of the 8 crystallographically inequivalent hydrogen sites of the

BETS molecule is mapped to a single line in the NMR spectrum, as shown in Fig. 1. The presence of a $y$ component of the field (along the $b$ axis) doubles the number of magnetically inequivalent hydrogen sites, which in turn splits the NMR peaks. A calculation using Eq. (1b) for the field in the $a^*b$ plane gives the separation

$$\Delta\nu \text{ [kHz]} = 0.32M \sin 2\beta$$

between the peaks from H-sites 8A belonging to the O-type and M-type BETS molecules, where $M$ is, as before, the magnetization (in emu/mol) and $\beta$ is the field polar angle measured from the $a^*$ direction. Similarly, the separation between the peaks from site 7A is

$$\Delta\nu \text{ [kHz]} = 0.014M \sin 2\beta.$$

This can be partially responsible for the difference in the linewidths of the peaks from H-sites 7A and 8A observed above 25 K (see Fig. 3) if we assume a small tilt of the goniometer axis from the normal to the field direction, which cannot be ruled out. For example, a 1° tilt would split the H-site 8A peak at 25 K, 1.4 T ($M = 1960$ emu/mol) by ±11 kHz, and the 7A site by ±0.5 kHz. However, the broadening of the peak from site 8A is observed instead of the splitting. To explain this, we introduce a small random displacement of the hydrogen positions and calculate the resulting peak positions using Eq. (1b). The calculations show that ±0.1 Å random displacement of hydrogen atoms from the listed crystallographic positions results in the standard deviation ±20 kHz of the peak positions for H-site 7A and ±37 kHz for H-site 8A. Convolved with the splitting from the 1° tilt, at $T = 25$ K, this gives the respective peaks of 20 kHz and 45 kHz half-linewidth for H-sites 7A and 8A, which is compatible with the data in Fig. 3. The linewidth in the metallic state therefore arises from a small random displacement of the hydrogen atom positions and a tilt $\sim 1°$ of the goniometer wheel.

Below $T_{MI} = 25$ K, the NMR peak widths sharply increase, indicating an enhancement of the local field scatter at hydrogen sites, which is no longer explained by the sample positioning and the atomic displacements. One of the options yielding an additional local field scatter below $T_{MI}$ is the AF order of $\pi$-electron spins inferred from the magnetic torque measurements [15]. For instance, in $\kappa$-$(ET)_2Cu[N(CN)_2]Cl$, the AF ordering of $\pi$-electrons causes a ±80 kHz splitting of the proton NMR peaks [19]. This is compatible with the observed width of the peak from H-site 7A at 4 K but is much smaller than the H-site 8A peak width (see Fig. 3). We therefore need to assume the ordering of $Mn^{2+}$ electron spins, as has also been suggested from dc magnetization measurements [15].

To roughly estimate the effect of the ordering of $Mn^{2+}$ moments on the proton linewidth, we have modeled two Mn sublattices with projections of the magnetic moment on the field direction, $(1 \pm \delta)\mu_{\text{Mn}}$, and calculated the dipolar field at hydrogen sites belonging to the O- and M-type BETS molecules (see Fig. 5) using Eq. (1b). The calculation gives the scatter of the proton frequences

$$\Delta\nu \text{ [kHz]} = 0.04M\delta$$

for H-site 7A and

$$\Delta\nu \text{ [kHz]} = 0.48M\delta$$

for H-site 8A. Taking $M = 5600$ emu/mol measured at $H = 1.4$ T and $T = 4$ K for $\delta = 0.25$, this respectively yields $\Delta\nu/2 = 30$ kHz and $\Delta\nu/2 = 330$ kHz for the scatter of the proton frequences at H-sites 7A and 8A, which is in a fair agreement with the measured half-linewidths.

The large difference in sensitivity of the local field scatter to the amplitude $\delta$ of the modulation of the $Mn^{2+}$ moment projection between H-sites 7A and 8A is graphically evident from the structure shown in Fig. 5. The local field at site 8A is strongly influenced by the magnetic moment of its single nearest neighbor Mn. In contrast, the hydrogen atom at site 7A has two nearly symmetric Mn neighbors. As a result, the difference in the magnetic moment projections of the neighboring Mn becomes essentially averaged at site 7A, which is observed as a much narrower peak in experiment.

Therefore, the increase of the linewidth below 25 K is mainly due to enhancement of the scatter of the static local field induced by an AF-type arrangement of the electron spins of $Mn^{2+}$. The shape of the $^1$H NMR spectrum below 25 K indicates a short- range or an incommensurate (or exotic) long-range AF order of $Mn^{2+}$ spins because otherwise, in the case of the long-range commensurate Néel order, the splitting would be observed instead of the broadening. The Néel order is probably not favorable in this system because manganese forms a triangular network in the anion layer. In such systems with the AF coupling, where the minimization of pairwise interactions is geometrically frustrated, exotic magnetic structures are often resolved in the ground state [20].

### 3.2. Spin–lattice relaxation

The $^1$H spin–lattice relaxation rate $T_1^{-1}$ was measured in $\kappa$-$(BETS)_2Mn[N(CN)_2]_3$ for the spectral peak

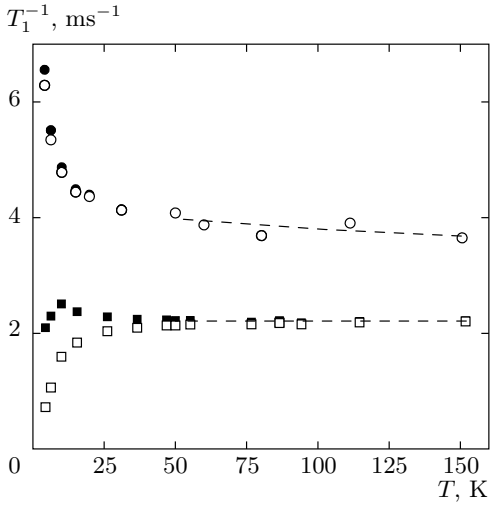


**Fig. 6.** Temperature dependence of the $^1$H spin–lattice relaxation rate for the spectral peak from H site 7A measured in $\mathbf{H} \parallel \mathbf{a}^*$ geometry at 1.4 T (circles) and 7 T (squares). Open symbols: raw experimental data. Filled symbols: experimental data divided by the polarization factor $1 - P_0^2$, $P_0 = M/M_0$. Dashed lines are splines for the data at $T > 50$ K

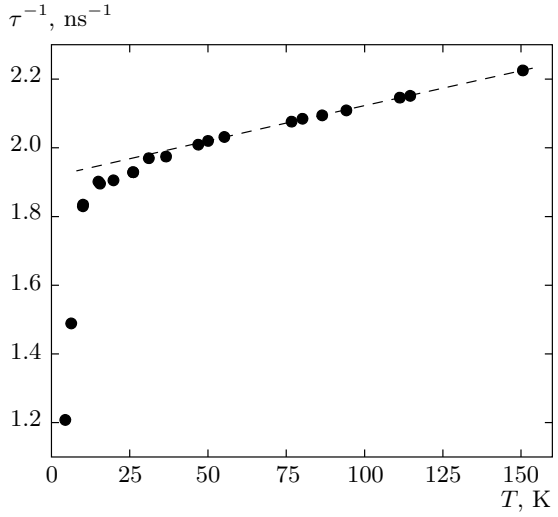


**Fig. 7.** Temperature dependence of the $Mn^{2+}$ electron spin–lattice relaxation rate extracted from the proton relaxation rate $T_1^{-1}$ (see Fig. 6) using Eqs. (3) and (4)

from hydrogen site 7A in the $\mathbf{H} \parallel \mathbf{a}^*$ geometry in fields 1.4 and 7 T. The NMR signal recovery after the inverting pulse followed the single-exponential $1-2\exp(-t_r/T_1)$ law. The measured values of $T_1^{-1}$ are plotted by open symbols as a function of temperature in Fig. 6.

It is readily seen from Fig. 6 that the proton spin–lattice relaxation in this system drastically differs from that in organic compounds with nonmagnetic anions (see, e. g., Ref. [19]). First, it is 3 to 4 orders of magnitude faster; second, it is strongly field dependent. To cope with the observed behavior of $T_1^{-1}$, we assume that the main source of the proton spin–lattice relaxation in $\kappa$-$(BETS)_2Mn[N(CN)_2]_3$ is the fluctuations of the local field at the hydrogen site caused by the spin–lattice relaxation process of the localized electron spins of $Mn^{2+}$. The well-known formula for the nuclear spin–lattice relaxation in this case is [21]

$$T_1^{-1} = F\frac{\tau}{1+(2\pi\nu\tau)^2}(1-P_0^2), \qquad (2)$$

where the prefactor $F$ is determined by the mutual arrangement of the nuclear and the electron spins, $\tau$ is the electron spin–lattice relaxation time, $\nu$ is the NMR frequency, and $P_0$ is the electron polarization. There are two field-dependent quantities in Eq. (2). One is the NMR frequency $\nu \approx \gamma_I H$. The other one is $P_0$, which accounts for the line-up of the electron moments at high fields (low temperatures), $P_0 = M/M_0$, where $M_0$ is the saturation value of the molar magnetization $M$. For $Mn^{2+}$ ($g$-factor 2, $J = S = 5/2$ ($L = 0$)),

$$M_0 = N_A g \mu_B J = 27912 \text{ emu/mol}.$$

The electron polarization can be easily accounted for by dividing the experimental data by the polarization factor $1 - P_0^2$. The corrected values

$$T_{1,corr}^{-1} = T_{1,exp}^{-1}/(1-P_0^2)$$

are plotted by filled symbols in Fig. 6. The ratio of the corrected $T_1^{-1}$ values at 1.4 and 7 T gives a simple equation quadratic in $\tau$:

$$R = \frac{T_{1,corr,1.4\,\mathrm{T}}^{-1}}{T_{1,corr,7\,\mathrm{T}}^{-1}} = \frac{1+(2\pi\tau\nu_{7\,\mathrm{T}})^2}{1+(2\pi\tau\nu_{1.4\,\mathrm{T}})^2}, \qquad (3)$$

where $\nu_{1.4\,\mathrm{T}}$ and $\nu_{7\,\mathrm{T}}$ are the NMR frequences at 1.4 and 7 T. Solving Eq. (3) for $\tau$, we obtain the electron spin–lattice relaxation time

$$\tau = \sqrt{\frac{1-R}{R(2\pi\nu_{1.4\,\mathrm{T}})^2 - (2\pi\nu_{7\,\mathrm{T}})^2}}\,. \qquad (4)$$

Figure 7 shows the temperature dependence of the $Mn^{2+}$ electron spin–lattice relaxation rate $\tau^{-1}$ extracted from the proton relaxation rate $T_1^{-1}$ using Eqs. (3) and (4). To reduce the scatter of the evaluated data, the experimental values of $T_1^{-1}$ above 50 K were

splined (as shown in Fig. 6 by a dashed line). At high temperatures, $\tau^{-1}$ is linear in $T$, which is natural for the phonon mechanism of the electron relaxation [22]. At some temperature between 16 and 25 K (close to $T_{MI}$), $\tau^{-1}$ turns down from the linear behavior. This loss of electron spin dynamics apparently signifies the freezing of $Mn^{2+}$ moments as the system enters the AF state.

## 4. CONCLUSION

We have performed a $^1$H NMR study of the organic conductor $\kappa$-$(BETS)_2Mn[N(CN)_2]_3$ above and below the MI transition that occurs at 25 K. The NMR spectra measured at different temperatures and magnetic field values and orientations agree very well with the model that assumes a dipolar field from the $Mn^{2+}$ moments at hydrogen sites. Vast broadening of the resonance peaks below 25 K has been shown to result mainly from a short-range or an incommensurate long-range AF order in the network of $Mn^{2+}$ ions. The commensurate long-range order is apparently absent because $Mn^{2+}$ forms a triangular lattice, which is unfavorable for a Néel-type arrangement. The proton spin–lattice relaxation has been shown to be dominated by fluctuations of the $Mn^{2+}$ electron spins. The electron spin dynamics evaluated from the proton $T_1^{-1}$ data is essentially suppressed below $T_{MI}$, which also indicates the freezing of $Mn^{2+}$ spin fluctuations.

This work was supported by the RFBR (grant No. 10-02-01202) and the DFG (grant No. RUS 113/926/0). The authors gratefully acknowledge the assistance in the questions of crystallography from R. P. Shibaeva, S. S. Khasanov, L. V. Zorina, and S. V. Simonov and the technical support from N. A. Belov.

## REFERENCES

1. E. Coronado and P. Day, Chem. Rev. **104**, 5419 (2004); T. Enoki and A. Miyazaki, ibid **104**, 5449 (2004); H. Kobayashi, H. Cui, and A. Kobayashi, ibid **104**, 5265 (2004).

2. L. Ouahab, in *Organic Conductors, Superconductors and Magnets: From Synthesis to Molecular Electronics*, ed. by L. Ouahab and E. Yagubskii, Kluwer Acad. Publ., Dordrecht–Boston–London (2003), p. 99.

3. G. Saito and Y. Yoshida, Bull. Chem. Soc. Jpn. **80**, 1 (2007).

4. E. Coronado and K. R. Dunbar, Inorg. Chem. **48**, 3293 (2009).

5. L. Ouahab and T. Enoki, Eur. J. Inorg. Chem. **2004**, 933 (2004).

6. S. Uji, H. Shinagawa, T. Terashima et al., Nature **410**, 908 (2001).

7. H. Fujiwara, H. Kobayashi, E. Fujiwara, and A. Kobayashi, J. Amer. Chem. Soc. **124**, 6816 (2002).

8. N. D. Kushch, E. B. Yagubskii, M. V. Kartsovnik et al., J. Amer. Chem. Soc. **130**, 7238 (2008).

9. V. N. Zverev, M. V. Kartsovnik, W. Biberacher et al., Phys. Rev. B **82**, 155123 (2010).

10. L. Brossard, R. Clerac, C. Coulon et al., Eur. Phys. J. B **1**, 439 (1998).

11. T. Sasaki, H. Uozaki, S. Endo, and N. Toyota, Synth. Metals **120**, 759 (2001).

12. M. Tokumoto, H. Tanaka, T. Otsuka et al., Polyhedron **24**, 2793 (2005).

13. C. Hotta and H. Fukuyama, J. Phys. Soc. Jpn. **69**, 2577 (2000).

14. F. Kagawa, K. Miyagawa, and K. Kanoda, Nature Phys. **5**, 880 (2009).

15. O. M. Vyaselev, M. V. Kartsovnik, W. Biberacher et al., Phys. Rev. B **83**, 094425 (2011).

16. G. Wu, P. Ranin, W. G. Clark et al., Phys. Rev. B **74**, 064428 (2006).

17. K. Kanoda, Hyperfine Interactions **104**, 235 (1997).

18. Cambridge Crystallographic Data Centre, www.ccdc.cam.ac.uk/data_request/cif, CCDC 775974-775977.

19. K. Miyagawa, A. Kawamoto, Y. Nakazawa, and K. Kanoda, Phys. Rev. Lett. **75**, 1174 (1995).

20. S. T. Bramwell and M. J. P. Gingras, Science **294**, 1495 (2001).

21. A. Abragam and M. Goldman, *Nuclear Magnetism: Order and Disorder*, Clarendon Press, Oxford (1982).

22. A. Abragam and B. Bleaney, *Electron Paramagnetic Resonance of Transition Ions*, Oxford Univ. Press, Oxford (1970).